Physics of Plasmas

Two-fluid electromagnetic simulations of plasma-jet acceleration with detailed equation-of-state

Cite as: Phys. Plasmas **18**, 103507 (2011); https://doi.org/10.1063/1.3647312
Submitted: 13 May 2011 . Accepted: 17 September 2011 . Published Online: 18 October 2011

C. Thoma, D. R. Welch, R. E. Clark, N. Bruner, J. J. MacFarlane, and I. E. Golovkin

View Online

Export Citation

ARTICLES YOU MAY BE INTERESTED IN

Hybrid-PIC modeling of laser-plasma interactions and hot electron generation in gold hohlraum walls
Physics of Plasmas **24**, 062707 (2017); https://doi.org/10.1063/1.4985314

Particle-in-cell simulations of collisionless shock formation via head-on merging of two laboratory supersonic plasma jets
Physics of Plasmas **20**, 082128 (2013); https://doi.org/10.1063/1.4819063

Integrated simulation of the generation and transport of proton beams from laser-target interaction
Physics of Plasmas **13**, 063105 (2006); https://doi.org/10.1063/1.2207587

AIP Publishing

© 2011 American Institute of Physics.

Two-fluid electromagnetic simulations of plasma-jet acceleration with detailed equation-of-state

C. Thoma,[1] D. R. Welch,[1] R. E. Clark,[1] N. Bruner,[1] J. J. MacFarlane,[2] and I. E. Golovkin[2]
[1]*Voss Scientific, LLC, Albuquerque, New Mexico 87108, USA*
[2]*Prism Computational Sciences, Inc., Madison, Wisconsin 53711, USA*

(Received 13 May 2011; accepted 17 September 2011; published online 18 October 2011)

We describe a new particle-based two-fluid fully electromagnetic algorithm suitable for modeling high density ($n_i \sim 10^{17}$ cm^{-3}) and high Mach number laboratory plasma jets. In this parameter regime, traditional particle-in-cell (PIC) techniques are challenging due to electron timescale and lengthscale constraints. In this new approach, an implicit field solve allows the use of large timesteps while an Eulerian particle remap procedure allows simulations to be run with very few particles per cell. Hall physics and charge separation effects are included self-consistently. A detailed equation of state (EOS) model is used to evolve the ion charge state and introduce non-ideal gas behavior. Electron cooling due to radiation emission is included in the model as well. We demonstrate the use of these new algorithms in 1D and 2D Cartesian simulations of railgun (parallel plate) jet accelerators using He and Ar gases. The inclusion of EOS and radiation physics reduces the electron temperature, resulting in higher calculated jet Mach numbers in the simulations. We also introduce a surface physics model for jet accelerators in which a frictional drag along the walls leads to axial spreading of the emerging jet. The simulations demonstrate that high Mach number jets can be produced by railgun accelerators for a variety of applications, including high energy density physics experiments. © *2011 American Institute of Physics*. [doi:10.1063/1.3647312]

I. INTRODUCTION

Plasma jets, loosely defined as collimated plasma structures with significant directed energy, occur in nature in the form of astrophysical jets,[1–3] which can be ejected from galactic cores, and solar prominences,[4] which are magnetized plasma loops which extend above the sun's surface. Plasma jets are also produced in the laboratory for both basic science research and applications. Laboratory jets can be generated by plasma guns,[5,6] in which a plasma load shorting a coaxial transmission line is driven by pulsed power. The plasma is accelerated to a high velocity by the resulting magnetic force. In a variation of this approach, coaxial transmission lines can be replaced by parallel plate electrodes.[7] Plasma jets can also be generated by the electrical breakdown of gas outside of a planar coaxial diode. After the initial breakdown, the resulting plasma becomes collimated and propagates in a direction normal to the diode plane.[8,9] Laboratory jets have also been generated by conical wire array explosions.[10] Applications for plasma jets include laboratory astrophysics,[11,12] spheromak formation,[8] pulsed plasma thrusters,[13,14] and disruption mitigation and refueling of magnetically confined fusion plasmas.[15]

Multiple converging plasma jets are also an attractive method for driving matter into high energy density regimes. At the plasma liner experiment (PLX)[16] at Los Alamos National Laboratory (LANL), a spherical array of up to 30 plasma jets will be used to create an imploding plasma liner which is expected to reach the regime of high energy density matter (pressure $\geq$0.1 Mbar). Such a liner could also ultimately be used to compress a magnetized target to fusion conditions in a scheme known as plasma jet-driven magneto-inertial fusion (PJMIF).[17–21] Some potential advantages of PJMIF over other inertial confinement fusion schemes are outlined in Ref. 22.

After exiting the accelerator, the jets have to traverse a standoff distance $\sim$1 m before they merge and form a liner around the target in PJMIF. Any expansion of the jets en route due to thermal spreading results in reduced stagnation pressure applied to the target. For this reason, it is desirable that the jets for this application be as cold as possible, or equivalently, have a high Mach number, M (ratio of directed to thermal speed for the jet). Awe *et al.*[23] have shown, in a series of 1D radial radiation-hydrodynamic simulations of liner compression, that the stagnation pressure of the liner scales as $\sim M^{1.5}$ for a wide range of plasma initial conditions. They have also demonstrated the strong beneficial effect of radiation cooling on Mach number, and hence stagnation pressure. Parks[24] has also demonstrated theoretically that ignition in PJMIF schemes requires very high Mach numbers for the incident jets. Although the thermal energy is a very small part of the total jet energy (on the order of 1%), for this particular application, the Mach number of the jet is an important figure of merit. This implies that a truly predictive modeling of plasma jet behavior for PJMIF applications requires the correct calculation of the plasma thermal energy. This requires the inclusion of non-ideal effects, such as ionization, excitation, and radiation processes which alter the specific heat of the plasma.

At PLX, the jets will be ejected from multiple railgun plasma jet accelerators developed by HyperV Technologies Corp.[25–27] A schematic drawing of a railgun accelerator is shown in Fig. 1. A pair of parallel metal plates serve as the electrodes of the accelerator. A pair of insulators on the sides

 © 2011 American Institute of Physics

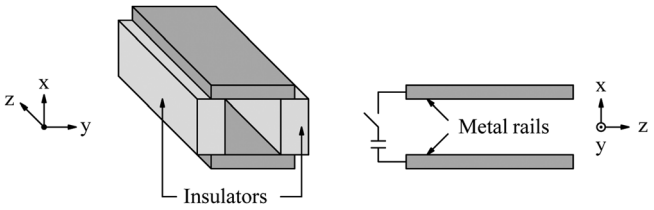

FIG. 1. Schematic illustration of the HyperV plasma railgun accelerator. The electrodes formed by the metal rails are 30 cm long in the z-direction and the accelerator aperture in the x-y plane, bounded by the electrodes and the insulators, is 1 cm × 1 cm.

form a square aperture for the plasma. The prototype accelerator is made with a 1 cm × 1 cm aperture, but, at PLX, jets will be created by railguns with larger apertures (1 sq in.). A localized high density pre-ionized plasma is injected into the upstream end of the 30-cm long accelerator. Both He and Ar gases have been used as sources of plasma. When the pulsed power circuit is closed, current runs along the electrodes with a return path provided by the plasma, which is accelerated by the $\vec{J} \times \vec{B}$ force at the plasma-vacuum interface. Jets emerging from railgun accelerators are found to have ion densities in the range of $n_i \sim 10^{16}$–10^{17} cm^{-3} and electron temperatures $T_e \sim 1$–5 eV.[25] However, measurements of initial plasma density at the upstream end of the accelerator can be significantly higher, reaching values $\sim 10^{18}$–10^{19} cm^{-3}. The acceleration of the plasma along the railgun, by magnetic fields on the order of a few Tesla, occurs on timescales on the order of a few μs, during which time the jets reach velocities ~50 km/s. On roughly the same timescales, the jets in PLX are expected to drift from the accelerator exit to a region in which the merging jets coalesce to form a liner. As they emerge from the end of the accelerator, the jets have transverse dimensions similar to the aperture size and an axial length ~10 cm.[27]

In such a parameter regime, traditional particle-in-cell (PIC) methods are impractical since the relevant length and timescales of the problem are much larger than the microscopic scales of the electrons which must be resolved in PIC codes. In this paper, we describe the algorithms which have been implemented in the code Lsp (Refs. 28 and 29) to facilitate the modeling of plasma jets. To demonstrate these new capabilities, we present simulation results in one and two Cartesian dimensions of plasma jet acceleration in the parallel plate railgun accelerator. In this paper, we restrict ourselves to accelerator simulations, but we note that the same algorithms enable simulations of a much wider class of problems in high energy density regimes including jet propagation and merging.

The main enabling algorithms are as follows. A fully electromagnetic (EM) implicit field solution combined with an energy-conserving particle advance allows simulations to under-resolve both electron timescales and lengthscales. When both ions and electrons are treated as fluid particle species, an Eulerian remap procedure allows simulations to be performed with one particle/cell/species. There is no assumption of quasi-neutrality and electron inertia is retained. In contrast to MHD, Hall physics is naturally included in the formulation. We have also applied an equation-of-state (EOS) modeling capability into a PIC framework. Rather than assuming a fixed charge state for ions and ideal gas behavior, electron internal energy, pressure, and the effective ion charge state of the plasma are given locally as functions of ion number, n_i, and electron temperature, T_e. These values are precalculated and stored in tabular form. Radiation effects can also be included as an electron energy sink due to emission in optically thin regimes. EOS and radiation effects are required to correctly describe the thermodynamics of jets and to accurately calculate jet Mach number. An electrode sheath model has also been implemented to model plasma-electrode interactions in multi-dimensional accelerator simulations.

These algorithms, which are described in greater detail in Sec. II, provide a new particle-based simulation capability which can be used to supplement existing MHD treatments[30,31] of plasma jet acceleration, transport, and merging. In Sec. III, we demonstrate the use of these algorithms in 1D and 2D simulations of Ar and He plasma jets in railgun accelerators. Conclusions are presented in Sec. IV where we also outline a general physical description of jet acceleration in parallel plate accelerators which is consistent with experimental measurements.

II. NUMERICAL ALGORITHMS FOR IMPLICIT PIC SIMULATIONS

We describe the algorithms used to accomplish relatively fast modeling of plasma jet phenomena. A brief description of the individual algorithms is given in the following subsections. The general flow of a complete simulation timestep advance, incorporating all of these algorithms, is given in Appendix A.

A. Direct-implicit field solution and fluid particle treatment

A direct-implicit solution for the electromagnetic fields allows accurate calculation for large timesteps: $\omega_{pe}\Delta t \gg 1$, where ω_{pe} is the electron plasma frequency. An energy-conserving particle push in concert with a cloud-in-cell[32] treatment allows large cell sizes: $\Delta x/\lambda_D \gg 1$, where λ_D is the Debye length. These algorithms are described in Ref. 29.

For plasma species that are well described by a Maxwellian velocity-space distribution, it is also possible to treat macroparticles as small discrete fluid elements.[33] Such particles still receive the same PIC Lagrangian particle push but, in addition to the Lorentz force and a frictional force due to Coulomb collisions, a pressure gradient force is included to account for thermal spreading. Each fluid particle also carries an intrinsic temperature. The temperature update includes terms for Ohmic heating, temperature equilibration, thermal conduction, and radiation losses. As opposed to a full kinetic treatment, this allows for simulations with fewer particles per cell, although detailed information on the local velocity distribution function is lost.

B. Equation of state and opacity calculations

The EOS and opacity data needed for the algorithms are pre-calculated by the Propaceos code,[34,35] which utilizes

detailed atomic models for plasmas in local thermodynamic equilibrium (LTE) as well as non-LTE states. In the present context, LTE means that the electrons have a "temperature" (i.e., Maxwellian distribution) and atomic level populations are determined by detailed balance. This state can be achieved when collisions dominate over radiative processes, so electron-impact excitation and deexcitation rates balance, as do electron-impact collisional ionization and 3-body recombination rates. It is not, however, assumed that $T_e = T_i$. So, the LTE approximation is consistent with the two temperature approach used. The EOS does, however, assume that quasi-neutrality holds, which is not guaranteed in the two fluid approach.

For LTE plasmas, atomic level populations are obtained from Boltzmann statistics and the ionic charge state distributions from the Saha equation. The effective charge state, $\bar{Z}_i$, is the mean ionic charge calculated from the full distribution of ionization stages $(0,1,\ldots,Z)$. Propaceos can also calculate non-LTE tables which should be used in regimes where the Boltzmann-Saha equilibrium does not occur, for example, if radiative or dielectric recombination dominates over three-body recombination. However, we have found that for the parameter regime considered here, non-LTE effects are negligible. In Appendix B, we present some representative EOS data for Ar and He in plasma jet conditions.

C. Implementation of equation of state into PIC framework

We now describe how the EOS data provided by the Propaceos tables is incorporated into a PIC framework with fluid particles. The intrinsic physical charge of a macroparticle (used to calculate the charge-to-mass ratio in the Lorentz force) is stored as a species attribute called Q_α, where $\alpha = e$ or i for electrons or ions, respectively, and is given in integral units of electron charge, $|e|$. Individual macroparticles of both species also carry a charge weight, q_α, which is proportional to the number of physical particles represented by the macroparticle. Ion macroparticles also carry an effective charge state $\bar{z}_i$. The corresponding charge state stored on the grid is denoted $\bar{Z}_i$ and is calculated from particle values of $\bar{z}_i$ by the usual weighting techniques used in PIC codes.[32] The grid quantity, $\bar{Z}_i$, represents the local average ionization state. Rather than carry a separate species for each ionization state, the non-integral particle attribute, $\bar{z}_i$, is carried by a single ion species and represents an effective multiplier of the intrinsic ion charge, $Q_i = 1$, in the Lorentz force. This can be seen explicitly in the ion momentum equation presented below. For electrons, the local charge-state is absorbed into the particle weight, q_e.

A quasi-neutral plasma is initialized by laying down collocated electron and ion macroparticles in grid cells. The initial e and i charge weights are related by the equality: $q_e = -\bar{z}_i q_i$, where $\bar{z}_i$ is calculated from EOS tables as a function of the initial values of ion density and electron temperature, n_i and T_e, respectively. We note that after the initialization, the electron and ion fluids can generate some charge separation, as the two fluid species are advanced in time. In practice, however, we find that ambipolar fields, which develop quickly compared to jet propagation timescales, suppress significant charge separation in all regions, except at the plasmas edges.

The ion and electron number density and the electron temperature are collected on the grid nodes. Once every time step, the grid values of $\bar{Z}_i$ and electron internal energy E_e are updated, by a call to the appropriate EOS table using the latest values of n_i and T_e. In the two-fluid treatment strict quasi-neutrality may be broken by the independent transport of electrons and ions. This can lead to cases where it is not possible to ensure strict charge conservation and to simultaneously impose exact local quasineutrality in the charge state update. In such cases, charge conservation takes precedence and the values of $\bar{Z}_i$ on the grid may be modified from the tabular value somewhat to prevent buildup of non-physical residual charge. As mentioned above, such cases occur only on the tenuous edges of the plasma.

The momentum and temperature advance of fluid macroparticles has been described in previous publications;[29,33] but we reconsider these issues here in order to emphasize the generalizations made to accommodate the EOS model. All macroparticles carry a velocity $\vec{v}_\alpha$, which is assumed to be non-relativistic for the jet applications considered in this paper. For fluid species, the velocity represents the directed motion of the macroparticle. Each macroparticle also carries an intrinsic temperature, denoted T_α. The corresponding grid temperatures are denoted T_α.

The momenta of electron and ion macroparticles are advanced by the Lagrangian force equations

$$\begin{aligned} \frac{d\vec{v}_e}{dt} &= Q_e \frac{e}{m_e}\left(\vec{E} + \frac{\vec{v}_e}{c} \times \vec{B}\right) - \frac{\nabla P_e}{n_e m_e} - \nu_{ei}\left(\vec{v}_e - \vec{V}_i\right), \\ \frac{d\vec{v}_i}{dt} &= Q_i \bar{z}_i \frac{e}{m_i}\left(\vec{E} + \frac{\vec{v}_i}{c} \times \vec{B}\right) - \frac{\nabla P_i}{n_i m_i} - \nu_{ie}\left(\vec{v}_i - \vec{V}_e\right), \end{aligned} \tag{1}$$

where $\vec{V}_\alpha$ is the grid drift velocity of a fluid particle of species $\alpha = e$ or i. This quantity as well as the electric and magnetic fields are stored on the grid nodes and interpolated to the particle position. Densities and temperatures are also stored on the grid. From these quantities, pressure gradients are calculated. In general, the electron pressure can be non-ideal and must in principle be obtained from EOS tables, but in the plasma jet parameter regime, we always find that $P_e \simeq n_e T_e$. The ions are always considered to be an ideal gas, with pressure $P_i = n_i T_i$. Note, as described above, in Eq. (1), the macroparticle effective charge state, $\bar{z}_i$, is applied to the charge-to-mass ratio in the Lorentz force for ions only.

The general Spitzer collision frequency for species α scattering off of species β is given by the formula[36]

$$\nu_{\alpha\beta} = \frac{4\sqrt{2\pi} e^4 Z_\alpha^2 Q_\alpha^2 Z_\beta^2 Q_\beta^2 \lambda_{\alpha\beta} n_\beta}{3 m_\alpha m_{\alpha\beta}} \left(\frac{T_\alpha}{m_\alpha} + \frac{T_\beta}{m_\beta}\right)^{-3/2}, \tag{2}$$

where Z_α is the charge state of species α, $m_{\alpha\beta} = m_\alpha m_\beta (m_\alpha + m_\beta)^{-1}$ is the reduced mass, and $\lambda_{\alpha\beta}$ is the Coulomb log.[37] Equation (2) is normally used for plasma species with a fixed integral value of Z. However, when the EOS model is invoked for an ion and electron species pair, Eq. (2) is used with $Z_e \to 1$ while the integer value of Z_i is replaced by the mean charge state $\bar{Z}_i$. To calculate the scattering terms on the

rhs of the momentum equations, the collision frequencies $\nu_{\alpha\beta}$ are also stored at the grid nodes and interpolated to the particle position. Everything needed to calculate the forces in Eq. (1) is stored on the grid prior to the momentum advance.

In the EOS model, the internal energy of the plasma is partitioned as follows. Ions are assumed to be ideal, so the grid ion internal energy (per unit ion mass) is given simply by

$$E_i = \frac{3}{2}\frac{T_i}{m_i}. \tag{3}$$

The grid electron internal energy, E_e, returned from Propaceos is also normalized per unit ion mass. For this reason, we choose to let the *ion* macroparticles carry the *electron* internal energy, ε_e. The electron and ion macroparticle temperatures are advanced in time as follows:

$$\begin{aligned}\frac{dT_e}{dt} &= \left(\frac{3\bar{Z}_i}{2m_iC_v}\right)\frac{2}{3}\left[-\frac{P_e\nabla\cdot\vec{V}_e}{n_e}+\frac{\nabla\cdot(\kappa_e\nabla T_e)}{n_e}\right.\\ &\left.+\ m_{ei}\nu_{ei}\left(\vec{V}_i-\vec{V}_e\right)^2+\mu_{ei}(T_i-T_e)+\frac{m_i}{\bar{Z}_i}\left(\dot{E}_e\right)_{\mathrm{rad}}\right],\\ \frac{dT_i}{dt} &= \frac{2}{3}\left[-\frac{P_i\nabla\cdot\vec{V}_i}{n_i}+\frac{\nabla\cdot(\kappa_i\nabla T_i)}{n_i}\right.\\ &\left.+\ m_{ie}\nu_{ie}\left(\vec{V}_i-\vec{V}_e\right)^2+\mu_{ie}(T_i-T_e)\right].\end{aligned} \tag{4}$$

The electron specific heat is given by

$$C_v = \frac{\partial E_e(n_i,T_e)}{\partial T_e}, \tag{5}$$

which is calculated on the grid and interpolated to the particle position. We note that the leading factor in parentheses on the *rhs* of the electron equation is unity for an ideal gas in a quasi-neutral plasma where

$$E_e \simeq \frac{3}{2}\bar{Z}_i\frac{T_e}{m_i}. \tag{6}$$

The temperature equilibration frequencies satisfy the equation

$$\mu_{\alpha\beta} = \frac{3m_{\alpha\beta}\nu_{\alpha\beta}}{m_\beta}, \tag{7}$$

and the thermal conductivity for electrons is related to the Spitzer frequency by

$$\kappa_e \propto \frac{n_eT_e}{m_e\nu_{ei}}, \tag{8}$$

with a similar expression for κ_i. We have neglected plasma viscosity effects and thermo-electric forces in Eqs. (1) and (4).

The electron energy equation contains an energy source term, $(\dot{E}_e)_{\mathrm{rad}}$, which accounts for emission/absorption of radiation. For relatively low temperature regimes ($\ll$keV), where radiation pressure can be neglected compared to plasma pressure,[38] there is no corresponding term in the momentum equation.

Photon absorption can be neglected when the photon mean free path, χ^{-1}, is long compared to the plasma size, L. In this (optically thin) regime, emitted photons simply free-stream out of the plasma without further interactions, and the radiation field acts as a pure electron energy sink, with

$$n_im_i\left(\dot{E}_e\right)_{\mathrm{rad}} = -c\kappa_eaT_e^4, \tag{9}$$

where a is the radiation constant and κ_e is the Gray Planck emission opacity (units cm^{-1}).[38] The Propaceos tables provide both κ_e and the Gray (frequency averaged) photon mean free path, χ^{-1} as a function of n_i and T_e. The timescale for radiation cooling of electrons is given by

$$\tau_C = -\frac{E_e}{\left(\dot{E}_e\right)_{\mathrm{rad}}}, \tag{10}$$

where $(\dot{E}_e)_{\mathrm{rad}}$ is calculated from Eq. (9).

In the opposite limit ($\chi L \ll 1$), it is necessary to include the effect of photon absorption as well as emission. This requires calculating the radiation energy density field, which is coupled to the plasma. For such optically thick regimes, a radiation transport model has been implemented in Lsp which self-consistently solves for the radiation field in the multi-group diffusion approximation.[38] In this regime, a photon absorption term must also be added to Eq. (9). In Appendix B, we demonstrate that the optically thin approximation is justified for jets in the parameter regime considered here.

D. Eulerian fluid algorithm

In addition to the fluid particle treatment described above, a species may also be designated as an "Eulerian" fluid. In this case, following the Lagrangian particle advance, particles are remapped back onto the Eulerian grid. The combination of the fluid-particle treatment and Eulerian remap allows simulations with ~1 particle/cell/species. For plasma-jet simulations, electrons are generally treated as an Eulerian fluid species, while ions can be treated either as a kinetic or fluid species. However, we assume fluid ions throughout.

The particles are remapped onto the Eulerian grid by the following procedure. All of the old particles are eliminated and a single new pair of particles (e and i) is laid down at each grid point, with new particle charges consistent with the grid values of density. New particle values of $\vec{v}_\alpha$, T_α, $\bar{z}_i$, and ε_e are also obtained from grid values. To conserve energy, any directed energy lost in the remap procedure is regained as thermal energy.

E. Sheath model

For multi-dimensional simulations, we have added an electrode plasma repopulation (sheath) model which can be applied at plasma-electrode interfaces in plasma accelerator simulations. The sheath algorithm is based on the following physical description. Ions which strike the electrode surface along a cell edge have a probability, $f_i \in [0,1]$, of liberating a neutral which is subsequently re-ionized. This neutral may be formed either by ion sputtering or the incident ion may recombine with an electron obtained from the wall. In either

case, an ion is lost and a neutral is generated near the electrode surface. When an existing particle strikes the electrode, a new electron and ion pair are ejected from the wall and placed at a random position in the cell adjacent to the wall. We have made the simplifying assumption that the reionization of the ejected neutral is essentially instantaneous. The newly created ion is also assumed to be composed of the same gas atom as the incident ion. For flexibility, both incident electrons and ions (with separate probabilities f_e and f_i) are allowed to stimulate electrode repopulation.

For incident ions, the normal velocity of the incident particle is retained and applied to the new pair (with a change in sign). The parallel velocity components of the new pair are given by some fraction, $\alpha \in [0,1]$, of the local ion drift velocity stored on the grid. For $\alpha < 1$, this results in an effective frictional force at the electrode surface. The surface is itself assigned a local temperature, T_S, and density, n_S. These values are used only to calculate EOS quantities for the newly created particles. If there are multiple incident particles striking a conducting cell boundary, the total charge is accumulated at the cell surface along with the (charge-weighted) average normal velocity. These aggregate values are then used to generate the properties of the new pair of particles. In addition to the physical picture for the repopulation model described above, for coarsely resolved $(\Delta x \gg \lambda_D)$ accelerator simulations some electrode repopulation is found to be necessary to suppress fast numerical magnetic penetration along the electrode surfaces. The effect of the sheath probabilities on jet acceleration is considered in greater detail in Sec. III B.

III. RESULTS

Simulation results are presented for both 1D and 2D Cartesian simulations of plasma jets in railgun accelerators. He is used as the gas in the 1D simulations and Ar is used for the 2D simulations.

A. 1D simulation results

We consider initially a simple 1D analog of the HyperV railgun accelerator in which the plasma has infinite transverse extent and some finite width density profile along the axis of propagation ($+x$ in this case). The magnetic field (aligned in the $+z$ direction) is established by injecting a TEM field from an open simulation boundary upstream of the plasma. After a linear temporal ramp, the magnitude of the upstream magnetic field remains constant in time and the plasma is accelerated in the $+x$ direction.

The ideal behavior of the 1D plasma jet can be determined by assuming that all acceleration is due to the $\mathbf{J} \times \mathbf{B}$ force.[5] This is a good approximation when magnetic pressure is large compared to mechanical pressure. We further assume that the plasma behaves essentially as a rigid body. In this case, the plasma has an acceleration of

$$a = \frac{B^2}{8\pi(m_j/A)}, \tag{11}$$

where B is the upstream vacuum field magnitude,

$$(m_j/A) = \int \rho_m(x)dx, \tag{12}$$

is the jet mass per unit cross-sectional area, A, and ρ_m is the plasma mass density. If we also assume a uniform mass density and axial jet length of w, Eqs. (11) and (12) can be simplfied to read

$$a = v_A^2/2w, \tag{13}$$

where

$$v_A = B/\sqrt{4\pi\rho_m}, \tag{14}$$

is the accelerator Alfvén velocity. The final jet velocity after propagating a distance L is simply given by

$$v_f = \sqrt{2aL} = \sqrt{\frac{B^2L}{4\pi\rho_m w}}, \tag{15}$$

where we have made use of Eqs. (13) and (14). We note that Eq. (15) gives the same general scaling of velocity with magnetic force $(v_f \propto I)$ as is observed in the plasma jets studied by Kumar and Bellan[39] for the purposes of spheromak generation.

Results from a typical 1D accelerator simulation are shown in Fig. 2. The figure shows snapshots of ion density and magnetic field strength as a function of x as a He jet is accelerated over a distance of about 30 cm, the length of the HyperV railgun accelerator. The top left of Fig. 2 shows the initial ion density profile of the jet which has a maximum value of 2×10^{17} cm^{-3}. For this simulation the EOS model is not used, a uniform ion charge state of $Z = 1$ is assumed, both ion and electron species are treated as ideal gases, and radiation losses are neglected. Both ion and electron species are treated as Eulerian fluids. The initial electron density profile is identical to that of the ions and, as the simulation is advanced in time, the initial quasi-neutrality is roughly maintained (as ambipolar electric fields suppress gross charge separation). Assuming a 1 cm $\times$ 1 cm cross-sectional area, as in the HyperV accelerator, the total jet mass $\sim$6.3 μg. Both ions and electrons are assigned an initial temperature of 5 eV (experiments at HyperV have found a range of temperatures from 1–5 eV in shots of the railgun accelerator). An initial drift velocity of 10 km/s in the $+x$ direction is assumed in the simulation. After a 500-ns linear ramp, the upstream magnetic field reaches a value of 3.3 T. The uniform cell size is $\Delta x = 0.1$ cm. A timestep of $c\Delta t = 0.0075$ cm is used. This timestep is constrained by the need to resolve the electron cyclotron frequency. We also note that reduced acceleration can occur in simulations if the electron collision frequency is significantly under-resolved.

The first observation to make about Fig. 2 is that the jet does not behave at all as a rigid body, as was assumed in the derivation of Eq. (11). At $t = 0.4$ μs (while the magnetic field is still rising), the initial effect of the input power on the leading edge of the plasma jet is a sharp compression of the density. The downstream side of the jet does not see the field at all but spreads out due to thermal effects. There is also a

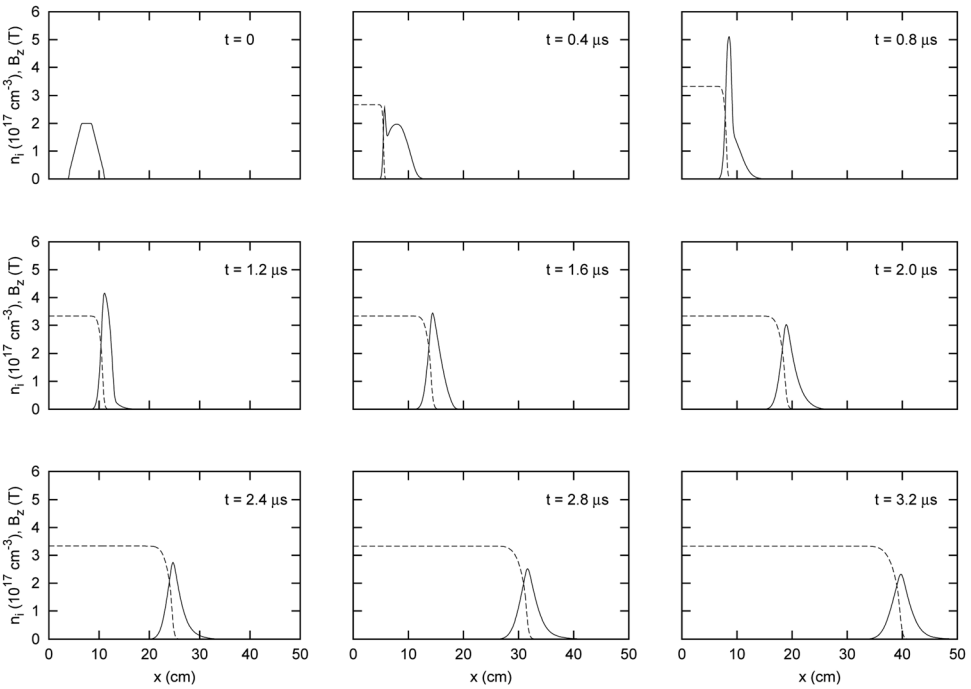

FIG. 2. Snapshots of ion density (solid line) and magnetic field (dashed line) as a function of x for a 1D Cartesian simulation of an accelerating He plasma jet. In this simulation, ions have a fixed charge state of +1 and both electrons and ions are assumed to be ideal gases. Radiation losses are neglected.

nominal amount of numerical diffusion inherent in the Eulerian fluid method which somewhat enhances the spreading of the plasma in simulation, but we believe this to be a small effect compared to the physical pressure gradient forces. At early times, there is negligible magnetic diffusion into the jet and the acceleration occurs only at the trailing edge, which compresses. In the fluid picture, information of the energy transferred to the trailing edge travels into the bulk of the jet only through the pressure gradient and scattering forces (fully kinetic simulations of the behavior at the trailing edge are discussed in Ref. 40). As the simulation progresses, the magnetic field diffuses into the jet region but this effect is balanced by the advection of the jet downstream. For this reason, the acceleration of the jet is able to continue for an extended period of time. We note that a similar axial compression on the trailing edge of an accelerating plasma jet has been seen experimentally by Yun and Bellan,[41] although in their experiment, the current and drift velocity of the jet are parallel rather than perpendicular, as is the case in a parallel plate or coaxial accelerator.

We estimate an average jet speed from the mean ion velocity, $\langle v_x(t)\rangle$, calculated from all ion macroparticles in the simulation space. After the initial 500 ns ramp on the drive power, the magnetic field reaches its full value of 3.3 T. For $t > 500$ ns, we find that the slope of $\langle v_x(t)\rangle$ has a constant value of 69 km/s/μs, in excellent agreement with Eq. (11). So we find that, in an average sense, Eq. (11) holds even for a non-rigid compressible jet. After 3 μs, the jet has reached an average speed of 200 km/s. We note that experiments at HyperV are generally performed with larger initial plasma masses than in the simulation results presented here. Mainly for this reason, experimental jet speeds have not yet been found to exceed ~50 km/s.

The simulation shown in Fig. 2 was performed with no EOS modeling (fixed ion charge state $Z = 1$ and ideal gas behavior) or radiation effects. We now repeat this simulation using the EOS model, both with and without the inclusion of radiation cooling. For these simulations, we have plotted both electron and ion density at several simulation times in Fig. 3. The results in the absence of radiation cooling are shown in plot (a). At $t = 0$, we find that $n_e/n_i \sim 1.5$ in the flat-top region of the jet. This is consistent with the table $\bar{Z}$ value for the initial conditions $n_i = 2 \times 10^{17}$ cm^{-3} and $T_e = 5$ eV. Despite the fact, the $n_e \neq n_i$, local charge quasineutrality is roughly maintained throughout the simulation. Plot (b) shows the same simulation results but with the inclusion of radiative electron cooling. When radiation cooling is included, the electron temperature in the jet drops rapidly (on a timescale of ~100 ns), in agreement with the cooling rates for He shown in plot (d) of Fig. 9 in Appendix B. As the electron temperature drops, the average charge state drops [plot (a) of Fig. 9].

The radiation cooling is significant because it can have a pronounced effect on the effective Mach number of the jet. This can be seen in Fig. 4, which shows plots of ion and electron densities and temperatures. Snapshots of three separate simulations are shown in the figure at $t = 3$ μs. Ion (solid lines) and electron (dashed lines) density profiles are plotted on the left y axis. The magnetic field profile in Tesla is also plotted on this axis. Ion (solid) and electron (dashed) temperatures are plotted on the right y axis. Simulation (a) uses singly-stripped ions with no EOS modeling or radiation cooling (as in Fig. 2). Simulation (b) includes EOS modeling with no radiation cooling. Simulation (c) repeats simulation (b) with radiation cooling included [some results from simulations (b) and (c) were already presented in Fig. 3]. A summary description of the three simulations can be found in Table I.

For all three simulations shown in Fig. 4, the plasma jet has reached approximately the same position, so the bulk acceleration is roughly the same for all cases. This is not surprising as the three simulations in the figure vary only in

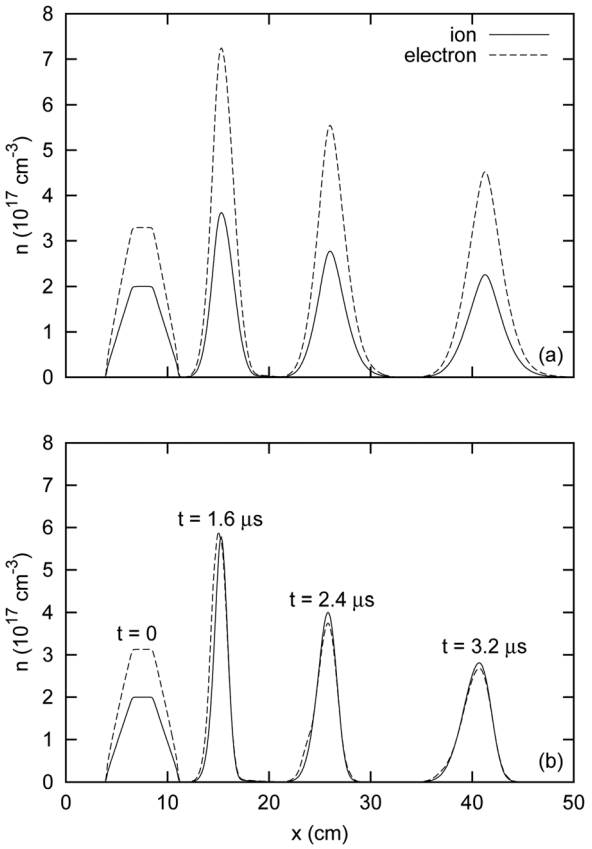

FIG. 3. Comparison of electron and ion densities at several times for 1D He accelerator simulations. Results are shown (a) without and (b) with inclusion of radiation cooling. The EOS model is used to calculate local values of ion charge state.

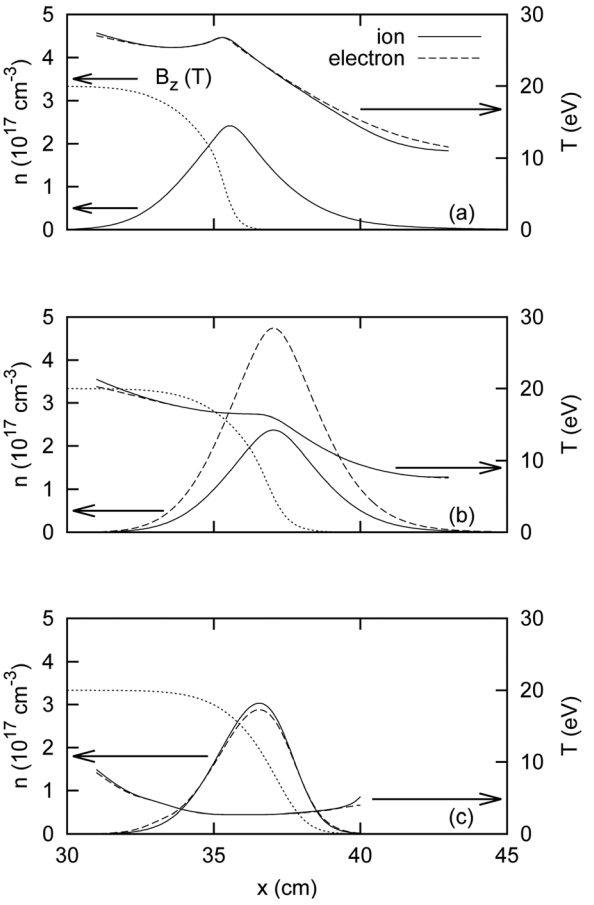

FIG. 4. Plots of ion and electron densities, temperatures, and magnetic field profiles (plotted on left axis) at $t = 3000$ ns for 1D He accelerator simulations. Results are shown for three separate simulations: (a) singly-stripped ions with no EOS modeling or radiation, (b) LTE EOS modeling with no radiation, and (c) LTE EOS modeling with radiation cooling.

their treatment of the internal energy (or temperature) of the plasma electrons. By definition, for a high Mach number jet, directed energy (due to the bulk acceleration by the magnetic field) $\gg$ internal or thermal energy. Moreover, the magnetic pressure at the plasma-vacuum interface greatly exceeds the mechanical pressure (required for efficient acceleration). As a result, the bulk acceleration is not too sensitive to the details of the plasma thermodynamics. Equivalently, the total directed velocity of the plasma depends mainly on the strength of the magnetic force. So the variations in Mach number seen in Table I are due only to changes in the calculated thermal energy of the plasma.

For each simulation, the ion and electron temperatures are very nearly equal in the bulk of the jet, as, at such densities, temperature equilibration due to electron-ion scattering can occur on μs timescales. For cases (a) and (b), which both neglect radiation cooling, the plasma temperatures are much higher than for case (c). The effective charge state (n_e/n_i) is correspondingly lower when radiation is included [compare cases (b) and (c)]. By similar arguments, there is less thermal spreading of the radiatively cooled jets as can be noted by comparing the jet widths for cases (a) and (b) with those of (c) and (d). This effect can also be seen in Fig. 5 which shows plots of ion $\langle v_x \rangle$ and $x_{\rm rms}$ as a function of time for the three simulations. All three simulations have nearly the same average velocity. After a transient time on the order of the temporal ramp on the field, the slope of $\langle v_x \rangle$ is in good agreement with Eq. (11) for all three simulations. But the rms value of x, a measure of the jet width, is somewhat smaller when radiation is included [case (c)].

For a uniform jet, the Mach number is calculated as

$$M = v/C_s, \tag{16}$$

where v is the jet speed and

$$C_s = \sqrt{\frac{\gamma \bar{Z} T_e}{m_i}}, \tag{17}$$

is the plasma speed of sound. The polytropic constant is defined as

TABLE I. Plasma jet parameters for 1D Cartesian He accelerator simulations at $t = 3000$ ns. Simulations (a)–(c) are identical to those described in Figs. 4 and 5. The values of T_e, $\bar{Z}$, and γ are calculated at $x = x_{\rm max}$.

	EOS	Rad. cooling	$x_{\rm max}$ (cm)	$\langle v_{xi} \rangle$ (km/s)	T_e (eV)	$\bar{Z}$	γ	M
(a)	No	No	35.6	199	26.6	1	5/3	6.1
(b)	LTE	No	37.05	203	15.9	2.0	1.32	6.4
(c)	LTE	Yes	36.6	197	2.7	0.95	1.17	24.5

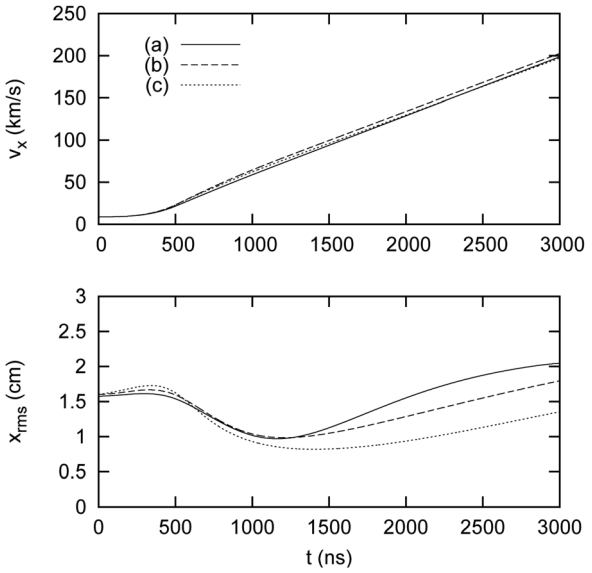

FIG. 5. History plots of ion $\langle v_x \rangle$ and $x_{\rm rms}$ for 1D He accelerator simulations. Results are shown for three separate simulations: (a) Singly-stripped ions with no EOS modeling or radiation, (b) LTE EOS modeling with no radiation, and (c) LTE EOS modeling with radiation cooling.

$$\gamma = \frac{P_e + P_i}{\rho_m \left(E_e + \frac{3T_i}{2m_i} \right)} + 1. \tag{18}$$

We estimate an effective Mach number for the simulation results by replacing v with the mean ion jet velocity at $t = 3$ μs. The other quantities in Eqs. (16)–(18) are calculated at the position of maximum ion density, $x_{\rm max}$, at that same time. The effective charge state, $\bar{Z}$ in Eq. (17), is calculated from the local value of n_e/n_i, rather than from grid values of $\bar{Z}_i$, although in practice, we always find that $n_e/n_i \simeq \bar{Z}_i$ in high density regions. The results for the three separate simulations are shown in Table I. All three simulations reach approximately the same speed, ~200 km/s, by $t = 3$ μs. But the effective Mach number is a factor of four higher when radiation cooling is included.

B. 2D simulation results

In this section, we describe results from 2D simulations of Ar jets in a parallel plate geometry. We now consider the case in which a plasma jet is placed in between electrodes with a plate separation of 1 cm (as in the HyperV railgun accelerator). The electrode sheath model described in Sec. II E is used to model the plasma electrode interface. The simulation geometry is shown in Fig. 6. The upper left plot shows the simulation space as well as a contour plot of the initial ion density. The maximum initial density is 2×10^{17} cm^{-3}. Both electrons and ions are given an initial temperature of 2 eV and an initial drift velocity of 10 km/s in the $+z$ direction. Electromagnetic power is fed into a wave-absorbing boundary at $z = 0$ upstream of the plasma. The plasma is accelerated in the $+z$ direction. The cathode and anode are located along the planes $x = 0$ cm and $x = 1$ cm, respectively. A perfectly conducting wall shorts out the cathode and anode in the plane $z = 30$ cm. The magnetic field ramps up to 3.3 T in 500 ns and points in the $-y$ direction. The cell size in the transverse direction is $\Delta x = 0.05$ cm, but a non-uniform grid is used in the axial direction with $\Delta z \sim 0.05$ cm at the initial location of the jet with the cells gradually expanding to a size of 0.1 cm at $z = 30$ cm. The time-step of $c\Delta t = 0.0075$ cm is again constrained by the electron cyclotron frequency. The sheath model is applied along both the cathode and anode surfaces with parameters: $f_e = 0.1$, $f_i = 0.9$, $\alpha = 0$, $T_S = 2.0$ eV, and $n_S = 10^{17}$ cm^{-3}. We find in practice, as expected, the behavior at the anode is largely unaffected by the value f_i, as mostly electron current flows into this electrode. Similarly, the cathode surface is relatively insensitive to f_e. The effect of the sheath model parameters is discussed in greater detail below.

The time evolution of the ion density can be observed in the contour plots of Fig. 6. At early times, $t < 1$ μs, the plasma evolves similarly to the 1D case. The plasma is compressed at the upstream vacuum interface. At later times, mass begins to gather near the electrode surfaces while a thin and more tenuous plasma armature maintains the current

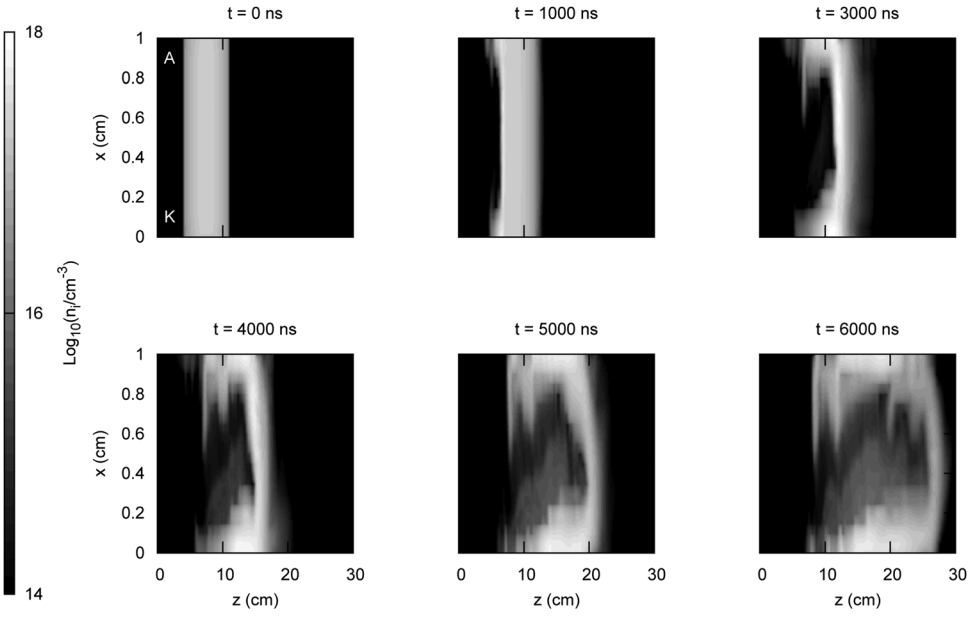

FIG. 6. Snapshots of ion density contours from Ar railgun acclerator simulation.

path between the electrodes. The plasma which builds up near the electrodes also loses axial speed relative to the armature and thus falls behind, as seen in the figure. This behavior occurs because the sheath model, as described in Sec. II E, builds in an intrinsic frictional drag with $\alpha = 0$, as the new particles are emitted from the electrodes without any of the axial velocity of the incident particles on the wall. There are also signs that the electrode plasma on the anode behind the armature attempts to restrike the cathode leaving thin density strands which appear to grow from the anode closer to the cathode in time. These strands do carry some current, however, as the magnetic field directly behind the armature in the center of the gap drops significantly from the vacuum value of 3.3 T as the simulation proceeds. The acceleration of the plasma armature no longer obeys the simple 1D formula of Eq. (11) due to the frictional electrode drag and the bulk movement of mass toward the electrodes.

Figure 7 again shows the ion density for the 2D Ar simulation at $t = 6$ μs as well as a contour plot of the ion axial velocity. We consider the local plasma parameters at four specific spatial locations for this simulation time. Points A and B are located well behind the armature near the anode and cathode surfaces, respectively. Point C is directly between the plates but slightly behind the armature, while point D is directly in the armature. Local plasma parameters for these four points are given in Table II. Both points A and B, along the electrodes, have higher ion densities than in the upstream armature (point D), but the velocities are much lower in these regions. At point C behind the armature, there is a high velocity but a much lower density. We note that

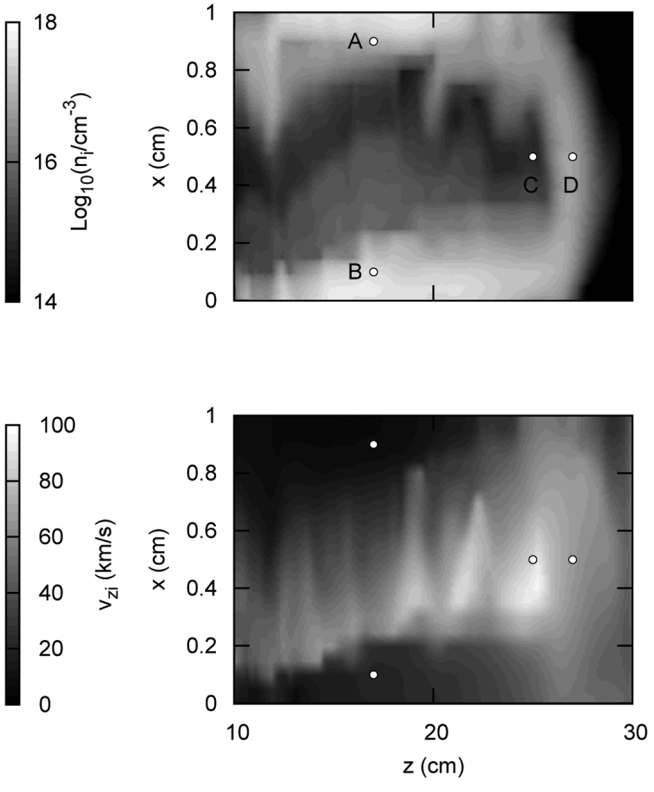

FIG. 7. Contour plots of (top) ion density and (bottom) ion axial velocity at $t = 6$ μs for an Ar railgun accelerator simulation.

TABLE II. Plasma parameters at different spatial positions (shown in Fig. 7) for 2D Cartesian Ar accelerator simulations at $t = 6000$ ns.

Position	n_i (cm^{-3})	Ion v_z (km/s)	T_e (eV)	$\bar{Z}$	γ	M
A	8.5×10^{16}	7	1.6	1.08	1.11	3.25
B	3.4×10^{17}	20	1.8	0.88	1.12	9.69
C	1.1×10^{15}	87	3.3	1.9	1.28	19.7
D	5.8×10^{16}	66	1.8	1.17	1.05	28.6

point C is at a density lower than the cutoff for the EOS table, and the calculated values of γ and $\bar{Z}$ are somewhat suspect as they are obtained by extrapolation. But the general conclusion remains the same: although there is a high velocity region behind the armature, the amount of mass there is quite small.

We see in Fig. 6 that the time evolution of the 2D jet is greatly affected by the electrode interactions which are simulated using the sheath model described in Sec. II E. Lacking at present a more comprehensive understanding of surface physics in the railgun accelerator, we seek to examine the sensitivity of the results to the sheath model parameters, f_e, f_i, and α. We note, first of all, the simulations require at least a moderate value for f_i. With $f_i = 0$, there is a rapidly evolving enhanced magnetic field penetration in the row of cells along the cathode surface in the simulation, which opens the circuit (in a manner similar to a plasma opening switch). This behavior is clearly non-physical since this effect is not observed in experiments with railgun jet accelerators.[25] We believe this behavior is the result of coarse gridding along the electrodes. The actual non-neutral sheaths which form along electrode surfaces are far too small (on the order of a Debye length) to be resolved over centimeter lengthscales. The rapid magnetic field penetration is the result of this gross under-resolution. But, numerically the cathode field penetration can be suppressed by setting f_i to a nonzero value (the minimum value of f_i required to suppress the field penetration is found to be dependent on the initial plasma parameters as well as the field strength and its local time derivative). When simulations are run with $f_e = 0$, the plasma density begins to decrease slightly along the anode surface. In contrast to the cathode, there is experimental evidence of such "anode starvation" in jet accelerators and thrusters,[42] so this effect may well be physical.

For the purposes of this paper, we treat f_e, f_i, and α as parameters and study the effects of varying these parameters. We consider four separate simulations with $\alpha = 0$: (a) $f_e = f_i = 0.5$, (b) $f_e = 0.05$ and $f_i = 0.5$, (c) $f_e = 0.25$ and $f_i = 0.75$, and (d) $f_e = 0.1$ and $f_i = 0.9$. Contours of ion density at $t = 5$ μs for each of the four simulations are shown in Fig. 8. We compare first cases (a) and (b) in the top row of Fig. 8. Both (a) and (b) are run with $f_i = 0.5$. There is a similar amount of plasma deposited on the cathode side in each. But in case (b), which has a much lower value of f_e, there is considerably less mass on the anode side than in case (a). It is important to note that quasineutrality is still roughly maintained in all of the snapshots in Fig. 8. There is no significant net charge density built up on the electrodes although the plasma mass density does indeed build up. We now consider

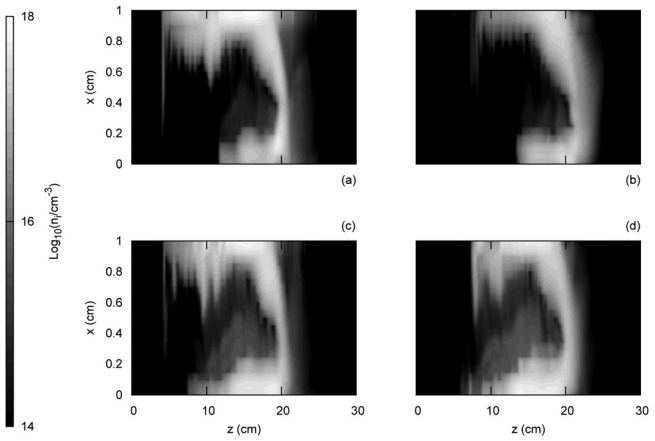

FIG. 8. Snapshots of ion density contours at $t = 5$ μs for 2D Ar simulations with varying sheath model parameters. (a) $f_e = f_i = 0.5$, (b) $f_e = 0.05$ and $f_i = 0.5$, (c) $f_e = 0.25$ and $f_i = 0.75$, and (d) $f_e = 0.1$ and $f_i = 0.9$.

together cases (a), (c), and (d). For all three of these cases, the sum $f_e + f_i = 1$. In proceeding from (a) to (c) to (d), the value of f_i is increased and the value of f_e is decreased. The general trend is that as f_i is increased and f_e is decreased, more mass builds up on the cathode side with less building up on the anode side.

We have also observed that, for the three simulations for which $f_e + f_i = 1$, the total simulation mass is roughly constant in time, as, on average, each electron and ion pair which leave the simulation are replaced by another pair. For case (b), the global mass decreases monotonically in time, as particles which are lost to the walls in order to maintain the current path are not fully replaced by the sheath model ($f_e + f_i < 1$). However, the total particle energy for case (b) is found not to be significantly lower than for the other cases which roughly keep the total mass constant. From this, we infer that most of the particle energy is in the leading plasma armature, with relatively little directed energy in the plasma built up on the electrodes behind the armature.

We have also considered the case in which the sheath model was run with $\alpha = 1$. This essentially eliminates all of the frictional drag on the electrodes. In this case, plasma mass still gathers up on the electrode surfaces, but does not fall behind the armature, as the frictional drag is absent. We note that we did not test the sensitivity of the model to the sheath parameters n_S and T_s, which were maintained throughout at their default values of 10^{17} cm^{-3} and 2 eV, respectively.

We propose the following explanation for the behavior of the jets with regard to the electrode sheath model parameters. We consider first the case with $\alpha = 0$ (maximum axial drag). Careful study of the early time behavior of the simulation shows that the plasma density begins to build up initially on the cathode surface. Ions are initially accelerated into the cathode by the transverse electric field which drives the current. We note that this is a polarity effect which would be absent in MHD. For $f_i > 0$, new ions born near the cathode surface are also accelerated back toward the cathode. This leads to a density buildup along the cathode. The resulting pressure gradient acts to push the plasma in the interior of the accelerator (i.e., off the cathode surface) in the direction of the anode. Moreover, for $\alpha = 0$, new particles born at either electrode from the sheath model lack the axial velocity component of the bulk jet and so begin to fall behind the interior plasma. This results in a distorted concave current path. For a concave shaped armature, the $\vec{J} \times \vec{B}$ force will have a component which drives mass toward each electrode surface, and a positive feedback condition occurs, leading to density profiles such as those seen in Fig. 8. When $\alpha = 1$, there is no effective axial drag on the plasma mass at the electrode surface but the mass still accumulates on both the cathode and anode surfaces by the polarity-driven seeding mechanism we have described above. The amount of mass which builds up on the electrodes is determined mainly by values f_e and f_i (see Fig. 8), and the amount of electrode frictional drag depends on the value of α.

If we again compare the four separate plots of Fig. 8, we see that for all cases the position, thickness, and density of the plasma armature away from the electrodes are roughly similar, which suggests that the armature formation and propagation in the *center* of the accelerator is roughly insensitive to the details of the sheath model. Mass is either lost to the walls (for $f_e + f_i < 1$) to carry current, or builds up on the electrode surfaces. The exact behavior of the plasma *on* the electrodes is strongly determined in the simulations by the values of f_e, f_i, and α.

IV. CONCLUSIONS

We have described the algorithms implemented into Lsp to enable the modeling of plasma jets and other high energy density physics phenomena and have demonstrated the use of these new techniques in 1D and 2D simulations of plasma jet simulations in a railgun geometry. In 1D simulations, in which no mass can escape in the transverse direction, the bulk jet acceleration is well estimated by the simple rigid body formula of Eq. (11), despite the very non-rigid behavior of the jets. We also demonstrated that the inclusion of EOS and radiation effects can strongly affect the calculated jet Mach number. For PJMIF schemes, high Mach number jets are required to reach high stagnation pressures in the liner formed by the merging of jets. For this reason, the inclusion of EOS and radiation effects is critical. For railgun simulations with He and Ar gases, we find the jets to be well approximated by an optically thin treatment of radiation in which absorption is neglected.

In 2D accelerator simulations, we considered the effect of plasma-electrode interactions on jet acceleration and found the behavior of the armature in the leading edge of the jet in the center of the accelerator to be relatively insensitive to the details of the surface physics model used on the electrodes. Based on these observations, we suggest the following scenario for the evolution of the jet in the railgun accelerator. A relatively large mass is injected into the upstream end of the accelerator. As the plasma is accelerated, some of the initial mass is lost to the electrodes to maintain the current path. There is also a buildup of mass along the walls, which is slowed down by frictional drag. A faster and more tenuous plasma maintains the armature away from the walls, leading to a concave current path. The

tenuous leading armature, which is relatively insensitive to the electrode conditions, emerges first from the 30-cm accelerator as the head of the propagating jet.

Although we did not explicitly simulate the detachment of the plasma from the accelerator, after 20–30 cm of propagation, we do obtain an Ar jet with a density of nearly 10^{17} cm^{-3} and a speed exceeding 60 km/s for a driving field of several Tesla, in general agreement with the results of experiments on the HyperV railgun accelerator.[27] HyperV also reports that significantly higher plasma densities are detected prior to the acceleration than in the jet which emerges from the accelerator.[27] We believe this density decrease results mainly from the mass loss which occurs for small effective values of f_e and f_i in the accelerator. The jets emerging from the end of the accelerator are also observed to have an axial profile which rises sharply at the leading edge and has a long tail in which the density falls off slowly,[43] with the total jet length on the order of 10 cm. This behavior can be explained by an effective electrode frictional drag ($\alpha < 1$) in the accelerator. In this case, the sharply rising head of the jet is due to the leading edge of the armature, and the tail is the slow electrode plasma which follows the leading edge.

The sheath model described in Sec. II E, although based on a physical argument, is still incomplete, as we lack any theoretical or experimental data to allow f_e, f_i, α, and other sheath model parameters to be estimated. Moreover, we have made the simplifying assumption in the model that plasma liberated from the electrodes is composed of the jet gas. Ideally, a more physics-based surface model is desired. Alternatively, the simulation results could be compared to experiments and the sheath model parameters varied to provide optimal agreement. Such analysis is outside the scope of this paper, which is limited to the introduction of the new algorithms and a demonstration of the new capabilities which they have enabled.

More extensive comparison with experiments will be the focus of future work. This will include simulation of the actual pulsed-power circuit used to drive the accelerator. The detachment of the plasma jet from the end of the accelerator can also be simulated. The simulation results can also be validated for jet propagation and merging by comparison with experiments to be conducted at PLX. In future work, we will also describe the generalization and optimization of these algorithms for operation in a hybrid mode in which electrons are fluid, but ions are treated kinetically and are allowed to retain multiple charge states. This allows detailed ion kinetics, such as finite mean-free-path effects, instabilities and turbulence, to be modeled. With these techniques incorporated, these algorithms would contain all the physics relevant for modeling a wide variety of high energy density plasmas.

ACKNOWLEDGMENTS

This work was supported by U.S. Department of Energy (DOE), Office of Fusion Energy Science (OFES), under Grant Number DE-FG02-05ER54835. The authors worked under subcontracts H008 (Voss) and H009 (Prism) of HyperV Technologies Corp. of Chantilly, Virginia. We gratefully acknowledge helpful conversations with Dr. Doug Witherspoon and Dr. Sarah Messer of HyperV, Dr. Jin-Soo Kim, Dr. John Thompson, and Dr. Nick Bogatu of Far-Tech, and Dr. Scott Hsu of LANL. We would also like to thank Dr. David Rose of Voss Scientific for his careful review of the paper.

APPENDIX A: ALGORITHM FLOW FOR TIMESTEP ADVANCE

In this appendix, we give a short schematic description of the full EM PIC direct-implicit algorithm for a single electron-ion EOS species pair. In the following, we list the sequence of events which occurs as the entire simulation domain is advanced by a single timestep.

1. The field is advanced in time by the timestep Δt by the direct-implicit algorithm.
2. Electron-ion particle pairs are created by the sheath model in cells along the electrode surface (as described in Sec. II E) based on the incident flux of particles accumulated during the previous timestep.
3. The following quantities are gathered on the grid based on the present particle values and locations: n_α, $\vec{V}_\alpha$, T_α, $\bar{Z}_i$, and E_e.
4. All of the fluid and scattering terms on the *rhs* of the momentum [Eq. (1)] and the temperature [Eq. (4)] equations are collected on the grid, including the electron radiation sink [Eq. (9)].
5. The particle momentum and temperature are updated by Eqs. (1) and (4). However, at this point, the Lorentz force is neglected and the particle position is not updated.
6. Values of $\bar{Z}_i$ and E_e are updated on the grid based on local values of n_i and T_e.
7. EOS quantities are scattered back to ion macroparticles ($\bar{z}_i$, ε_e) from grid quantities ($\bar{Z}_i$, E_e).
8. The particles are remapped onto the Eulerian grid by the procedure described in Sec. II D. Particles which are placed onto the electrode boundaries are added as incident particles for the sheath model in the subsequent timestep.
9. Particle momenta are now updated by the Lorentz force and the particle positions are advanced as well. Particle contributions to the current density are gathered on the grid.

APPENDIX B: EOS QUANTITIES FOR HE AND AR PLASMA JETS

In this appendix, we present some data from LTE EOS tables for He and Ar. The tables are constructed to cover the density range from 10^{16}–10^{25} cm^{-3} and the temperature range from 10^{-2}–10^{3} eV. The opacity tables are constructed with 10 frequency groups with photon energies extending from 0.1 to 10^5 eV. Some EOS and radiation quantities for He are shown in Fig. 9 as a function of electron temperature for ion densities from 10^{16} to 10^{19} cm^{-3}. The mean charge-state, $\bar{Z}$, is shown in plot (a) of Fig. 9. The mean charge state

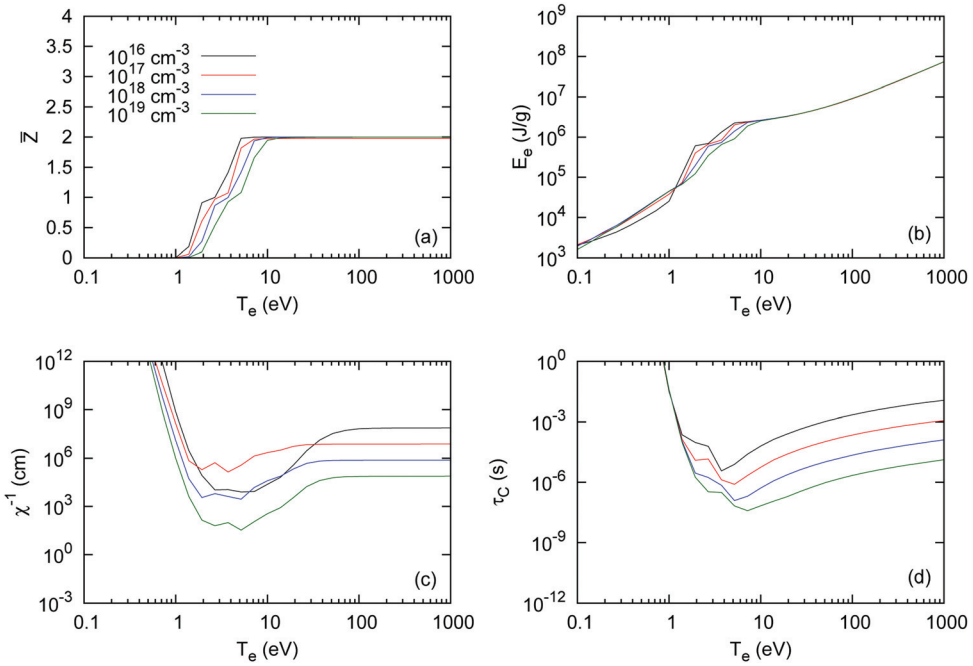

FIG. 9. (Color) EOS and radiation quantities for He in the density regime of plasma jet accelerators (10^{16}–10^{19} cm^{-3}). (a) Mean ion charge-state, (b) electron internal energy, (c) photon mean free path, and (d) electron radiation cooling time are plotted as a function of T_e.

is seen to be negligible for temperatures less than an eV and rises monotonically with temperature until it is fully stripped for T_e on the order of 10 eV. Plots (c) and (d) of Fig. 9 show the photon mean free path, χ^{-1}, and electron cooling time, τ_C [Eq. (10)]. Plot (c) demonstrates that, for the densities considered, the photon mean free path does not approach the centimeter lengthscales of the PLX plasma jets. So He may be considered essentially optically thin during plasma jet acceleration. By contrast, plot (d) shows that the electron cooling time in the temperature range from 1–5 eV can approach the microsecond timescales over which jets are accelerated for densities $>10^{17}$ cm^{-3}. In this regime, it is adequate to treat He jets as optically thin with a pure electron energy sink due to radiation emission. The same general behavior is observed for the EOS of Ar in the jet regime considered in this paper. Namely, for densities lower than about 10^{18} cm^{-3}, Ar can be treated as an optically thin radiation emitter in LTE.

In this paper, we consider only plasma jet acceleration, but in PLX, individual plasma jets will be merged to form a liner and much higher densities are expected. In such regimes, radiation absorption may be significant. We also note that the opacity data in Fig. 9 are constructed with only 10 frequency groups. By averaging the opacity data over a small number of finite-width bins, some frequency dependent effects are not included in the analysis. For example, the effect of strong line radiation can be smeared out over a wide frequency bin.

[1]W. H. T. Vlemmings, P. J. Diamond, and H. Imai, Nature (London) **440**, 58 (2006).
[2]Y. Kato, Astrophys. Space Sci. **307**, 58 (2006).
[3]M. Nakamura, H. Li, and S. Li, Astrophys. J. **656**, 721 (2007).
[4]J. Chen and J. Krall, J. Geophys. Res. **108**, 1410, doi:10.1029/2003JA009849 (2003).
[5]J. Marshall, Phys. Fluids **3**, 134 (1960).
[6]T. D. Butler, I. Hennis, F. C. Jahoda, J. Marshall, and R. L. Morse, Phys. Fluid **12**, 1904 (1969).
[7]T. E. Markusic, E. Y. Choueiri, and J. W. Berkery, Phys. Plasmas **11**, 4847 (2004).
[8]S. C. Hsu and P. M. Bellan, Phys. Rev. Lett. **90**, 215002 (2003).
[9]S. You, G. S. Yun, and P. M. Bellan, Phys. Rev. Lett. **95**, 045002 (2005).
[10]S. C. Bott, S. V. Lebedev, D. J. Ampleford, S. N. Bland, J. P. Chittenden, A. Ciardi, M. G. Haines, C. Jennings, M. Sherlock, G. Hall, J. Rapley, F. N. Beg, and J. Palmer, Phys. Rev. E **74**, 046403 (2006).
[11]P. M. Bellan, S. You, and S. C. Hsu, Astrophys. Space Sci. **298**, 203 (2005).
[12]S. V. Lebedev, J. P. Chittenden, F. N. Beg, S. N. B. A. Ciardi, D. Ampleford, S. Hughes, M. G. Haines, A. Frank, E. G. Blackman, and T. Gardiner, Astrophys. J. **564**, 113 (2002).
[13]R. Jahn, *Physics of Electric Propulsion*, 1st ed. (McGraw-Hill, New York, 1968).
[14]K. Schoenberg, R. Gerwin, I. Henins, R. Mayo, J. Seuer, and G. Wurden, IEEE Trans. Plasma Sci. **21**, 625 (1993).
[15]A. Voronin, V. Gusev, Y. Petrov, N. Sakharov, K. Abramova, E. Sklyarova, and S. Tolstyakov, Nucl. Fusion **45**, 1039 (2005).
[16]S. C. Hsu, F. D. Witherspoon, M. A. Gilmore, and J. Cassibry, Bull. Am. Phys. Soc. **54**(15) (2009), available at: http://meetings.aps.org/link/BAPS.2009.DPP.TP8.149.
[17]Y. Thio, E. Panarella, R. Kirkpatrick, C. Knapp, F. Wysocki, P. Parks, and G. Schmidt, *Current Trends in International Fusion Research-Proceedings of the Second Symposium* (NRC Research Press, Canada, Ottawa, 1999), chap. Magnetized Target Fusion in a Spheroidal Geometry with Standoff Drivers, pp. 113–131.
[18]Y. Thio, C. Knapp, R. Kirkpatrick, R. Siemon, and P. Turchi, J. Fusion Energy **20**, 1 (2001).
[19]Y. C. F. Thio, C. Knapp, R. Kirkpatrick, R. Siemon, and P. Turchi, J. Comput. Phys. **20**, 1 (2002).
[20]Y. C. F. Thio, J. T. Cassibry, and T. E. Markusic, in *AIAA Joint Propulsion Conference*, Paper No. AIAA-2002-3803, (AIAA, 2002).
[21]Y. Thio, J. Phys.: Conf. Ser. **112**, 042084 (2008).
[22]S. C. Hsu, J. Fusion Energy **28**, 246 (2008).
[23]T. J. Awe, C. S. Adams, J. S. Davis, D. S. Hanna, S. C. Hsu, and J. T. Cassibry, Phys. Plasmas **18**, 072705 (2011).
[24]P. B. Parks, Phys. Plasmas **15**, 062506 (2008).
[25]F. D. Witherspoon, R. Bomgardner, A. Case, S. J. Messer, S. Brockington, L. Wu, R. Elton, S. Hsu, J. Cassibry, and M. A. Gilmore, Bull. Am. Phys. Soc. **54**(15) (2009), available at: http://meetings.aps.org/link/BAPS.2009.DPP.TP8.150.

[26]F. D. Witherspoon, R. Bomgardner, A. Case, S. Messer, S. Brockington, L. Wu, R. Elton, S. Hsu, J. Cassibry, and M. Gilmore, Bull. Am. Phys. Soc. **55**(15), 358 (2010), available at: http://meetings.aps.org/link/BAPS.2010.DPP.UP9.111.
[27]F. D. Witherspoon, S. Brockington, A. Case, S. Messer, and R. Elton, Rev. Sci. Instrum. (to be submitted).
[28]Lsp was developed by ATK Mission Research Corporation with initial support from the Department of Energy (DOE) SBIR Program.
[29]D. R. Welch, D. V. Rose, M. E. Cuneo, R. B. Campbell, and T. A. Mehlhorn, Phys. Plasmas **13**, 063105 (2006).
[30]J. Cassibry, Ph.D. thesis, University of Alabama in Huntsville, 2004.
[31]J. Loverich and A. Hakim, J. Fusion Energy **29**, 532 (2010).
[32]C. K. Birdsall and A. B. Langdon, *Plasma Physics Via Computer Simulation* (Adam Hilger, New York, 1991).
[33]D. R. Welch, D. V. Rose, N. Bruner, R. E. Clark, B. V. Oliver, K. D. Hahn, and M. D. Johnston, Phys. Plasmas **16**, 123102 (2009).
[34]J. J. MacFarlane, I. E. Golovkin, and P. R. Woodruff, J. Quant. Spectrosc. Radiat. Transf. **99**, 381 (2006).
[35]J. J. MacFarlane, I. E. Golovkin, P. Wang, P. R. Woodruff, and N. A. Pereyra, High Energy Density Phys. **3**, 181 (2007).
[36]P. W. Rambo and R. J. Procassini, Phys. Plasmas **2**, 3130 (1995).
[37]H. L. Anderson (Ed.) "A Physicist's Desk Reference, 2nd Edition", American Institute of Physics, New York 1989. Specifically Chapter 18 (p. 278) written by D. L. Book.
[38]G. C. Pomeraning, *The Equations of Radiation Hydrodamics* (Dover, Mineola, New York, 2005).
[39]D. Kumar and P. M. Bellan, Phys. Rev. Lett. **103**, 105003 (2009).
[40]C. Thoma, D. R. Welch, and T. P. Hughes, Phys. Plasmas **16**, 032103 (2009).
[41]G. S. Yun and P. M. Bellan, Phys. Plasmas **17**, 06108 (2010).
[42]E. H. Niewood, Ph.D. thesis, Massachussets Institute of Technology, 1993.
[43]S. J. Messer, private communication, 2011.